



# Automated classification of granular bainite and polygonal ferrite by electron backscatter diffraction verified through local structural and mechanical analyses

R. M. Jentner<sup>1</sup>, S. P. Tsai<sup>1,2</sup>, A. Welle<sup>3</sup>, S. Scholl<sup>4</sup>, K. Srivastava<sup>4</sup>, J. P. Best<sup>1</sup>, C. Kirchlechner<sup>1,5</sup>, G. Dehm<sup>1,a)</sup>

<sup>1</sup>Max-Planck-Institut Für Eisenforschung GmbH, Max-Planck-Straße 1, 40237 Düsseldorf, Germany

<sup>2</sup>Department of Materials Science and Engineering, National Taiwan University, Roosevelt Road 1, Taipei 10617, Taiwan

<sup>3</sup>Karlsruhe Nano Micro Facility and Institute of Functional Interfaces, Karlsruhe Institute of Technology, 76021 Karlsruhe, Germany

<sup>4</sup>AG der Dillinger Hüttenwerke, Werkstraße 1, 66763 Dillingen/Saar, Germany

<sup>5</sup>Institute for Applied Materials, Karlsruhe Institute of Technology, 76344 Eggenstein-Leopoldshafen, Germany

<sup>a)</sup>Address all correspondence to this author. e-mail: dehm@mpie.de

Received: 25 January 2023; accepted: 10 July 2023

**Differentiation of granular bainite and polygonal ferrite in high-strength low-alloy (HSLA) steels possesses a significant challenge, where both nanoindentation and chemical analyses do not achieve an adequate phase classification due to the similar mechanical and chemical properties of both constituents. Here, the kernel average misorientation from electron backscatter diffraction (EBSD) was implemented into a Matlab code to differentiate and quantify the microstructural constituents. Correlative electron channeling contrast imaging (ECCI) validated the automated phase classification results and was further employed to investigate the effect of the grain tolerance angle on classification. Moreover, ECCI investigations highlighted that the grain structure of HSLA steels can be subdivided into four grain categories. Each category contained a different nanohardness or substructure size that precluded a nanoindentation-based phase classification. Consequently, the automated EBSD classification approach based on local misorientation achieved a reliable result using a grain tolerance angle of 5°.**

## Introduction

High-strength low-alloy (HSLA) steels are widely used in several applications, e.g., constructions or pipelines, thanks to their mechanical and technical properties (e.g. weldability) [1–4]. This type of steel is commonly composed of a complex mixture of polygonal ferrite, degenerated pearlite, bainite, and residual martensite-austenite constituents. The volume fraction, distribution, and morphologies of these individual phases greatly influence the overall mechanical properties [5–8]. It is supposed that granular bainite can only form during continuous cooling, which is compared to an isothermal heat treatment widely used in the industrial production process [9]. Granular bainite is defined as a composition of irregular ferrite having irregular grain boundaries and a carbon-rich second phase which is distributed between the irregular ferrite grains and commonly composed of degenerated pearlite or martensite/

retained austenite [1]. This is caused by the increasing carbon concentration within the austenite during the continuous cooling process, which stabilizes the austenite and leads to the formation of carbon-rich austenite [10]. Moreover, the formation of polygonal and irregular ferrite leads to a decreasing austenite phase fraction and thus, the carbon concentration further increases within the untransformed austenite and forms various carbon-rich second-phase constituents [10, 11]. However, it has been found that the transformation range of the individual constituents partly overlap during the continuous cooling process which aggravates the phase classification [12–14].

It is a challenging task to discriminate between irregular ferrite and polygonal ferrite, since both are characterized by a granular morphology and, for example, light optical microscopy (LOM) does not have sufficient resolution to reveal the differences [9, 15]. From transmission electron microscopy (TEM)

investigations, irregular ferrite is subdivided by small ferrite sheaves or equiaxed grains depending on the applied cooling rate [3, 9, 16]. In addition, one further characterizing feature is the absence of carbides between the irregular ferrite substructure that further impedes differentiation between irregular and polygonal ferrite [9]. However, TEM investigations do not allow statistical phase analysis due to the limited investigated volumes. As a result, scanning electron microscopy (SEM) has been used to obtain reference images and texture parameters from isothermally produced samples. The images and texture data were implemented into a support vector machine [17]. The ideal structures were well characterized by this approach, but it remains challenging to capture the whole variety of the individual constituents [3, 13, 18].

In comparison, electron backscatter diffraction (EBSD) has been used as a powerful tool to identify phases and perform orientation analyses. EBSD shows no difficulty in differentiating austenite from ferrite, but it remains a challenge to distinguish lath bainite from martensite, or granular bainite from polygonal ferrite, since these phases only exhibit little tetragonality from the body-centered cubic (bcc) phase. As a result, studies show that these phases demonstrate similar microstructural morphologies and misorientation distributions [3, 15, 19]. Despite the difficulties, previous studies reported that granular bainite grains exhibit a higher misorientation within the grain compared to polygonal ferrite [15, 16, 20]. This is caused by the onset of a displacive transformation which governs the granular bainite formation, and it can only be accommodated plastically by geometrically necessary dislocations. This indeed offers an opportunity for phase identification between granular bainite/polygonal ferrite. In fact, researchers have proposed different methodologies, broadly applying either grain- or pixel-based parameters [19, 21, 22]. Zaefferer et al. [23] compared in detail the pattern quality, grain reference orientation deviation, and kernel average misorientation (KAM) to characterize the bainitic and ferritic phases and concluded that only the pixel-based KAM value gives a reliable separation of the bainitic and ferritic phase [23].

Based on the study of Keehan et al., an orientation gradient of  $3^\circ$ – $6^\circ$  per  $10\ \mu\text{m}$  was first defined by point-to-origin measurements to distinguish between granular bainite and polygonal ferrite [20]. Later, Chen et al. [15] correlated the orientation gradient within the individual grain and the KAM to achieve a reliable phase classification of granular bainite and polygonal ferrite. Moreover, the impact of a different step size and kernel size (kernel size = step size \* n-th nearest neighbor) was studied and it was found that the kernel size has to be comparable to the substructure size, and in that case further refinement of the step size does not play an important role to reveal the optimal classification of both constituents. In terms of the misorientation threshold, it was further suggested that a grain with an orientation gradient larger than  $3^\circ$  counts as granular bainite and is thus

independent of the measured length; this was related to the fact that the correct kernel size covers several bainite sub-units and can exceed  $3^\circ$ . Within this study [15], a grain tolerance angle of  $10^\circ$  was used to define the grain boundary. However, it has been shown that polygonal ferrite grains of a deformed material can be also subdivided by boundaries with a misorientation smaller than  $10^\circ$  [24]. Zhu et al. [25] determined that the effective grain size correlates well with the inverse lath size of bainite using a boundary misorientation angle of  $2^\circ$ – $7^\circ$ . This additionally indicates that the application of a smaller grain boundary tolerance angle may better represent the mechanical strength level of the individual constituent. However, a phase separation and quantification based on the KAM threshold has not yet been automated and validated by correlative investigations.

In addition to using EBSD-based parameters to characterize the selected HSLA steel, nanoindentation and chemical analysis have been employed here to assist in differentiation of the constituents. Specifically, nanoindentation tests were used to separate bainitic ferrite containing carbon-rich precipitates between the substructure and ferrite according to the measured hardness [26]. A phase classification using nanoindentation remains challenging for both lath bainite and martensite, as well as granular bainite and polygonal ferrite due to the comparable mechanical properties [27]. Electron probe microanalysis (EPMA) has been used to differentiate ferrite and martensite according to their carbon concentration [28, 29]. However, the carbon concentration caused by the electron beam required extensive experimental effort to minimize carbon contamination and achieve reliable carbon differentiation. Subsequently, the present study considered Time-of-Flight Secondary Ion Mass Spectrometry (ToF-SIMS) analysis as a possible tool to test whether different carbon concentrations between the constituents can be resolved as ToF-SIMS has a sufficient high lateral resolution (approx.  $0.1\ \mu\text{m}$ ) to resolve individual grains and phases. In addition, the detection limit for light elements, which is within 6 ppm, is also high enough, since atom probe tomography experiments showed that irregular ferrite grains contain a carbon concentration of 50 to 750 ppm [30–32]. However, ToF-SIMS has not yet been used to distinguish granular bainite from polygonal ferrite.

To the authors' best knowledge, an automated phase differentiation and quantification of granular bainite and polygonal ferrite using EBSD-based KAM mapping has not yet been developed. An additional feature of this work is the subsequent correlative electron channeling contrast imaging (ECCI) investigations and point-to-origin measurements of the orientation gradient within the grain interior to validate and adjust the characterization tool. Figure 1 schematically illustrates the classification process from the EBSD measurement until the automated phase identification and the conducted analysis to validate the achieved results. The classification system was tested on a rolled HSLA steel containing granular bainite and polygonal ferrite.

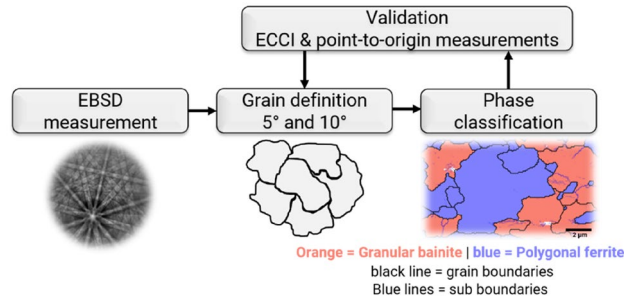


**Figure 1:** Schematic illustration of the classification process. After performing the EBSD measurement, the grains were defined by a grain tolerance angle of 5° and 10°. Both constituents, polygonal ferrite and globular bainite were separated using a KAM threshold of 3°. ECCI and point-to-origin measurements were conducted to validate the achieved results.

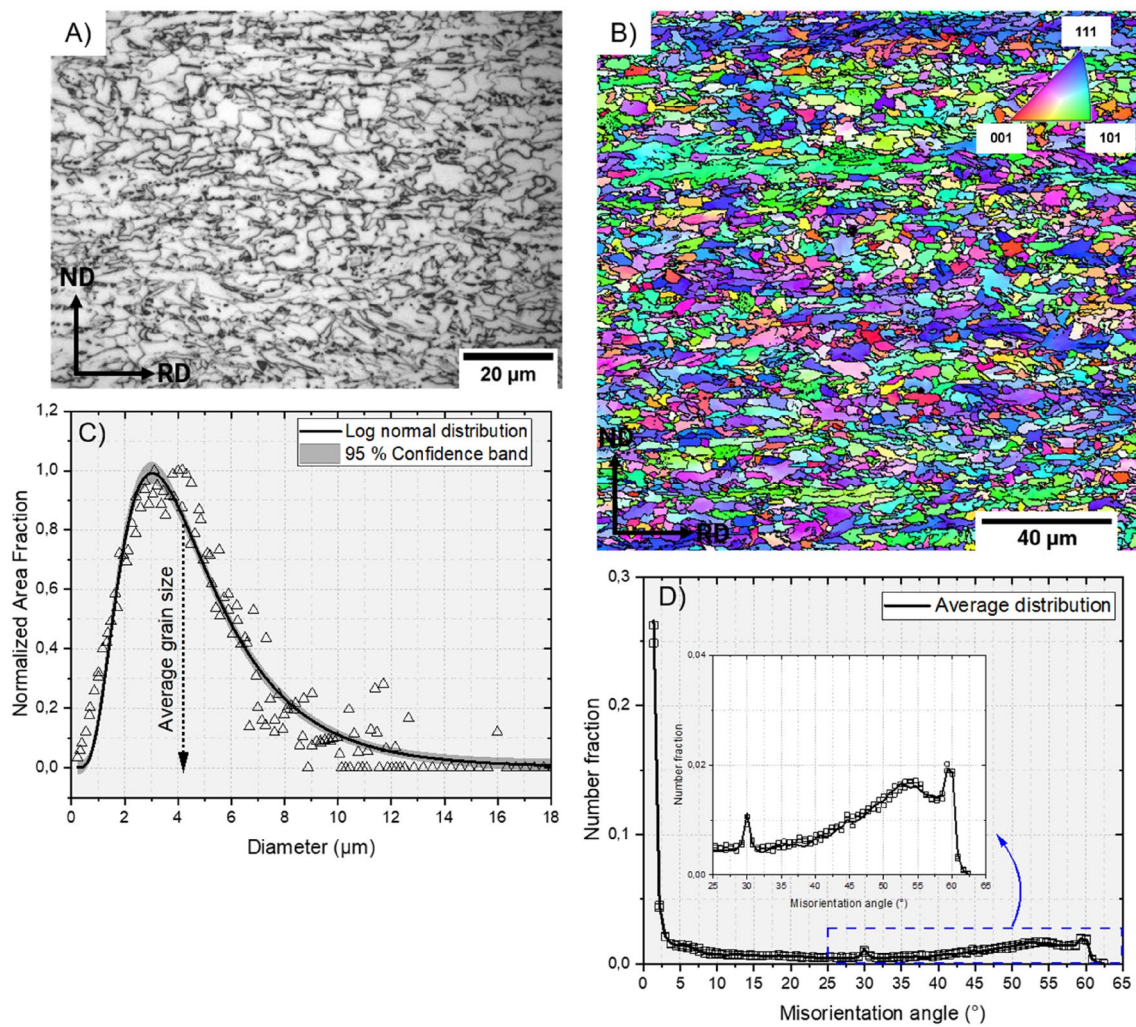


**Figure 2:** (A) Representative LOM image of the investigated microstructure. Both  $80 \times 80 \mu\text{m}^2$  scan areas were taken along the transverse direction and is illustrated by the IPF image (B). (C) and (D) show the grain size distribution, fitted using a log–normal function, and the average misorientation angle distribution of both scan areas.

## Results and discussion

### Preliminary microstructural characterization

The investigated microstructure is illustrated by a LOM image in Fig. 2(A) and the inverse pole figure (IPF) in Fig. 2(B). The polygonal and irregular ferrite grains in Fig. 2(A) are white etched, whereas the dark-etched carbon-rich second phase was identified as degenerated pearlite and martensite/retained austenite islands. The microstructural features of degenerated pearlite and martensite/retained austenite were not separately considered within this study due to their size and comparable consistency to irregular ferrite within the EBSD dataset (see “Influencing aspects” section). Consequently, the phase classification and quantification by EBSD will only distinguish between polygonal ferrite and granular bainite, including the carbon-rich second phase.

The IPF image within Fig. 2(B) provides detailed information regarding the microstructural complexity. The grain boundaries defined by a tolerance angle of  $5^\circ$  are displayed as black lines. The grains are elongated along the rolling direction and fine structured. Two representative  $80 \times 80 \mu\text{m}^2$  scan areas were used to calculate the grain size and misorientation angle distribution, as shown in Fig. 2(C) and (D). The grain size distribution [Fig. 2(C)] was fitted using a log-normal function and revealed an average grain size of  $4.2 \pm 0.6 \mu\text{m}$ . It was not possible to separate both constituents by LOM, since the resolution is too low to resolve the sub-sheaves of the irregular ferrite grains.

A further indication that the investigated material consists of polygonal ferrite and granular bainite is given by the misorientation angle distribution shown in Fig. 2(D). The characteristic misorientation angle distribution of a granular bainite microstructure is described by a high misorientation angle fraction below  $20^\circ$  and a broad distribution around  $45^\circ$  [1]. Since this is in accordance with our observation, it was concluded that the investigated material contains granular bainite. The small peak at  $30^\circ$  is related to mis-indexed pixels (pseudosymmetry) and can have different origins which are explained in detail elsewhere [22]. The morphology, grain size, and misorientation angle distribution did not allow for distinguishing between granular bainite and polygonal ferrite grains, hence further EBSD analyses were conducted.

Point-to-origin measurements have been suggested as a further suitable characterization technique to separate both constituents according to the orientation gradient [10, 15, 16, 20]. Chen et al. [15] utilized those measurements to measure the orientation gradient inside the grains and differentiated both constituents according to a misorientation threshold of  $3^\circ$ . Consequently, point-to-origin measurements were also performed to characterize 22 selected grains. With respect to the  $3^\circ$  threshold, nine grains (PF-1–PF-9) were classified as polygonal ferrite (see Fig. 3(A)) and 13 grains (GB-1–GB-13) as granular

bainite as the misorientation was below or above the selected  $3^\circ$  threshold, respectively [see Fig. 3(B)]. The point-to-origin measurement procedure is shown in Fig. 3(A–B) by two representative grains (PF-5 and GB-2). The formation history of each constituent is responsible for the different orientation gradient inside the grains. Polygonal ferrite grains start to nucleate at the prior austenite grain boundaries and the reconstructive transformation does not typically include large strain gradients inside the grain interior [9, 24, 33]. Granular bainite nucleates also at the prior austenite grain boundaries and forms a substructure due to the displacive transformation. This has been proven by TEM investigations [9, 34, 35]. The continuous cooling process leads to the formation of shear stresses which are relaxed by geometrically necessary dislocations (GNDs) and the associated formation of sub-grain boundaries [36, 37]. Accordingly, the 22 selected grains can be manually categorized using the point-to-origin measurement method. Subsequently, further nanoindentation tests were utilized to validate these results. In comparison to the distinct classification according to the misorientation, the load and depth curves in Fig. 3(C) illustrate that the nanoindentation tests did not allow a clear phase separation due to the continuous transition of the load and depth curve. Only grain GB-2 shows a higher hardness compared to the other tested grains. Subsequently, an average nanohardness of polygonal ferrite and granular bainite and reduced Young’s modulus were measured according to the classification by the orientation gradient; the results are summarized in Table 1. A previous investigation revealed that the bainitic yield stress is proportional to the inverse lath size of sub-boundaries defined by a boundary misorientation of  $2\text{--}7^\circ$  [25]. Therefore, a different bainitic substructure could explain different hardness levels but not the similar mechanical response of the polygonal ferrite grains. Further investigations were conducted to clarify this phenomenon and will be presented in “Mechanical properties of four different grain categories” section.

The chemical composition, specifically the carbon content of the steel, was also considered for achieving a separation of both constituents. Since granular bainite is formed by a displacive transformation which hinders carbon diffusion, attempts were made to measure the differences in carbon concentration between polygonal ferrite and granular bainite by ToF-SIMS. Due to air contact of the samples, their topmost layer contains many different air-borne hydrocarbon contaminations. Therefore, the samples were sputter cleaned *in vacuo* directly before imaging using a low energy  $\text{Cs}^+$  beam. Organic contaminations were removed easily, as observed by the rapidly dropping hydrocarbon signals and increasing signals of iron oxo clusters, and erosion of the material underneath was kept below approx. 1 nm due to the low sputter ion energy and dose. Furthermore, cesium ions implanted in the sample surface increase the ionization yield of negative secondary

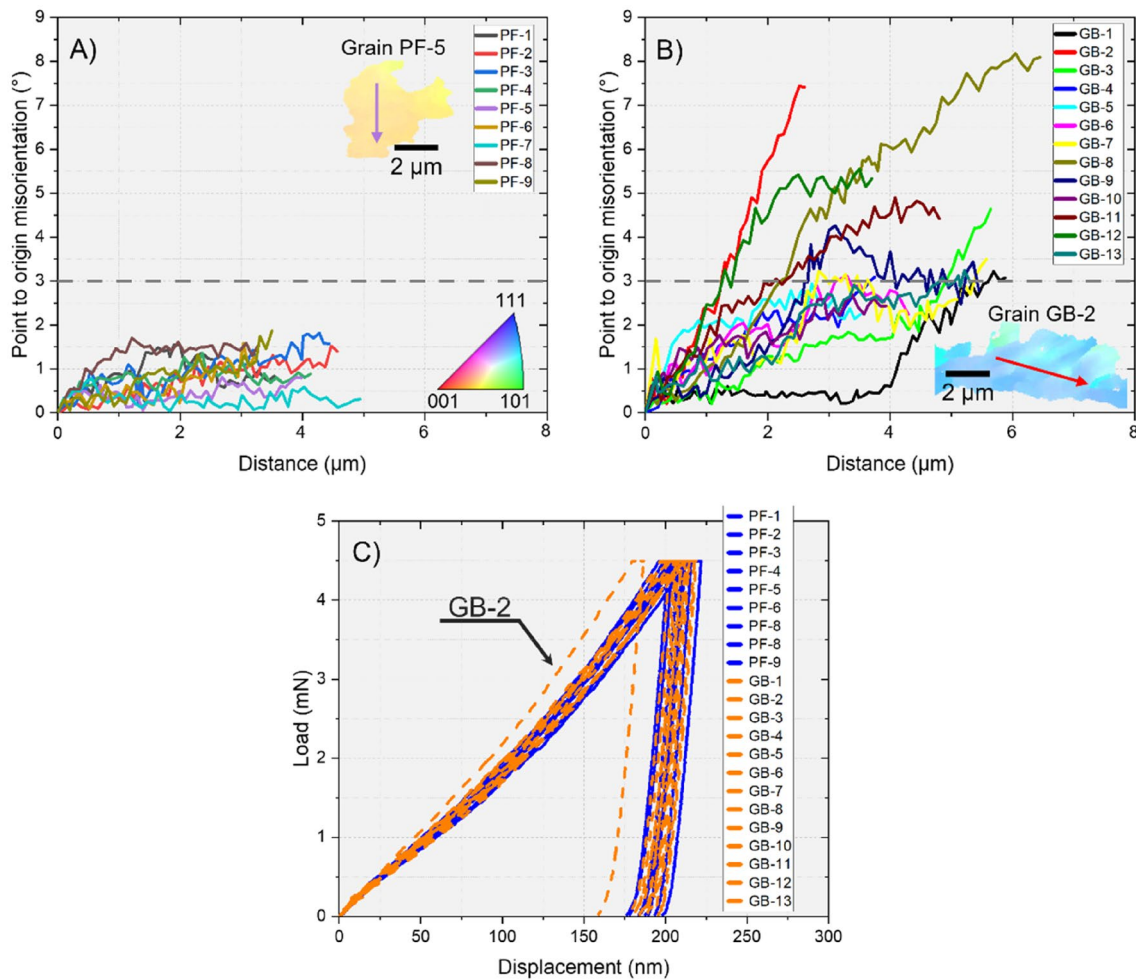


**Figure 3:** Based on the measured misorientation inside 22 selected grains were nine grains (PF-1 to PF-9) classified as polygonal ferrite (A) and thirteen grains classified as granular bainite (B). (A) and (B) additionally contain two representative examples (PF-5 and GB-2) to illustrate the point-to-origin measurement (colored arrow). The 3° threshold to separate both phases is marked as a gray-dashed line. The nanoindentation load and depth curves of the 22 tested grains (C) did not allow a classification between both constituents; only grain GB-2 showed a distinct separation. The nanoindentation results of all 22 tested grains are given in the “Supplementary Information”.

**TABLE 1:** Summary of the calculated average hardness and reduced Young’s modulus obtained by nanoindentation. The grains were classified as polygonal ferrite and granular bainite according to the EBSD misorientation measurements.

Phase	Avg. $H$ [GPa]	Stand. dev. [GPa]	Avg. $E_r$ [GPa]	Stand. dev. [GPa]	# indents
Polygonal ferrite	2.6	0.1	192	9	9
Granular bainite	2.7	0.1	198	15	13

ions used for subsequent imaging. Figure 4(A) shows the lateral distribution of the carbon concentration measured on a representative scan area-based secondary ions ( $C^-$ ,  $CH^-$ ,  $C_2^-$ ,  $C_2H^-$ ,  $C_3^-$ ,  $C_4^-$ ) superimposed with the grain boundary structure (grain tolerance angle 5°) which were obtained from

the EBSD measurement. Single hydrogen containing species can arise due to adsorption of hydrogen from the residual atmosphere in the spectrometer’s recipient. The logarithmic intensity scale of the carbon concentration additionally highlights smaller values and indicates a homogeneous carbon distribution overall the grain areas. Only a few small spots with a higher carbon concentration were detected and assigned to artifacts on the sample surface or to the lasting imprint of a diamond Berkovich indenter. Moreover, two representative grains (PF-5 and GB-8) were marked and characterized by EBSD point-to-origin measurements; the approximate position of the point-to-origin measurement is indicated by the blue arrow within each grain. One can recognize that PF-5 and GB-8 were identified according to the maximum misorientation as polygonal ferrite and granular bainite, respectively [shown in Fig. 4(B)]. It has been proven that ToF-SIMS is

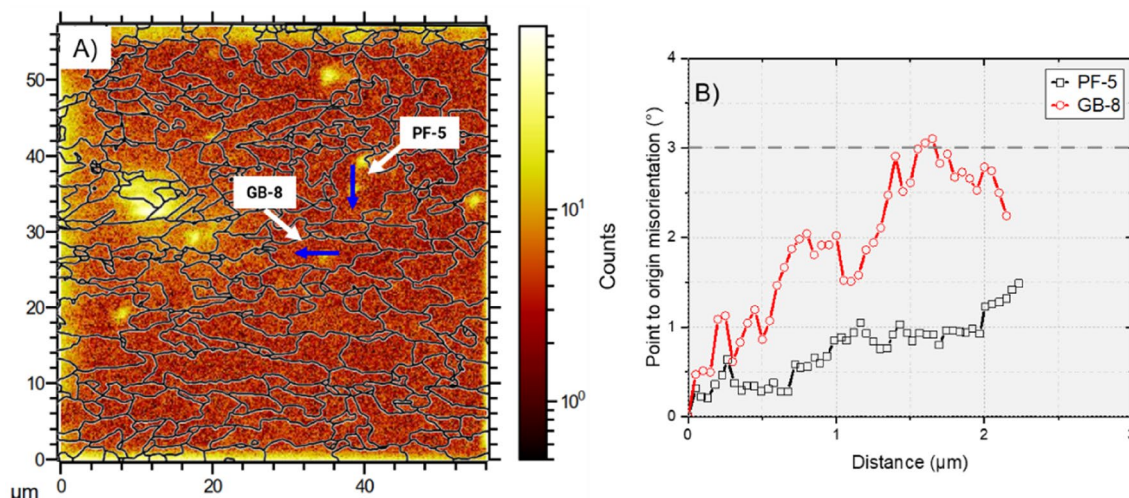


**Figure 4:** (A) shows a representative ToF-SIMS scan area and the lateral intensity distribution of summed signals of  $C^-$ ,  $CH^-$ ,  $C_2^-$ ,  $C_2H^-$ ,  $C_3^-$ , and  $C_4^-$ . In addition, the superimposed grain boundary structure (grain tolerance angle  $5^\circ$ ) was obtained from the EBSD measurement and illustrated by black lines. (B) The representative polygonal ferrite (PF-5) and granular bainite (GB-8) grains were characterized by measuring the orientation gradient with point-to-origin measurements.

capable to reach a mass and lateral resolution of 6 ppm and 100 nm for light elements, respectively [30, 31]. As a result, ToF-SIMS had originally been thought to be able to resolve the investigated microstructure and different carbon concentrations between the constituents. However, previous studies pointed out that at lower cooling rates the carbon atoms are still able to diffuse away from the ferrite–austenite interface, which leads to a larger carbon gradient within the residual austenite [38]. Hence, the reduced carbon saturation impedes the formation of carbon precipitates between the sub-blocks and only small quantities of retained austenite/martensite or degenerated pearlite are formed depending on the degree of carbon enrichment [10, 38]. Thus, it was not possible to identify individual grains according to their carbon concentration as the representative SIMS measurement shows.

These experiments further illustrate the difficulty to reveal a reliable phase classification of such microstructures with similar properties using either chemical or mechanical approaches. Since point-to-origin measurements showed a clear separation of the selected grains, the KAM and the  $3^\circ$  threshold were used to create an automated classification workflow. These results in terms of phase separation and quantification on the tested material, as well as the corresponding validation studies, are presented below.

### Automated phase classification and quantification

The developed Matlab® code uses the MTEX toolbox [39] to define first the grain boundaries according to the selected grain tolerance angle and afterwards calculate the KAM

affiliated with each pixel. The program classifies grains as granular bainite if one pixel exceeds a misorientation of  $3^\circ$ ; otherwise it is categorized as polygonal ferrite. Subsequently, the classification algorithm color-codes the classified grains according to their determined phase and calculates the measured granular bainite and polygonal fraction. Figure 5(A) displays the automatically calculated results (from two  $80 \times 80 \mu m^2$  scanned areas) by varying the kernel sizes (100–600 nm) and additionally compares the differences between the grain tolerance angle of  $5^\circ$  and  $10^\circ$ . The granular bainite fraction continuously increases with increasing the kernel size and shows a transition point at 330 nm and 350 nm using a grain tolerance angle of  $5^\circ$  and  $10^\circ$ , respectively. The transition point was identified using a linear equation to fit the datapoints with the best  $R^2$ -squared factor ( $R^2 = 0.99$  in all eight cases). Chen et al. [15] manually identified a constant kernel size range of 300–600 nm as the optimal kernel size to determine a reliable granular bainite fraction, which fits well to our detected transition points. It is assumed that the optimal kernel size will capture the information from several sub-units if it is in the range of a single sub-unit and allows an appropriate phase classification. A kernel size being too large will cover the whole area of small ferrite grains and cause an incorrect classification [15]. This is related to a higher dislocation density near the ferrite boundaries, which originates from strain accommodation of the bainitic displacive transformation [9]. The detection of a transition point could be related to a different substructure size between the investigated material and the literature results. Subsequently, the transition point was also identified as an indicator to determine the optimal

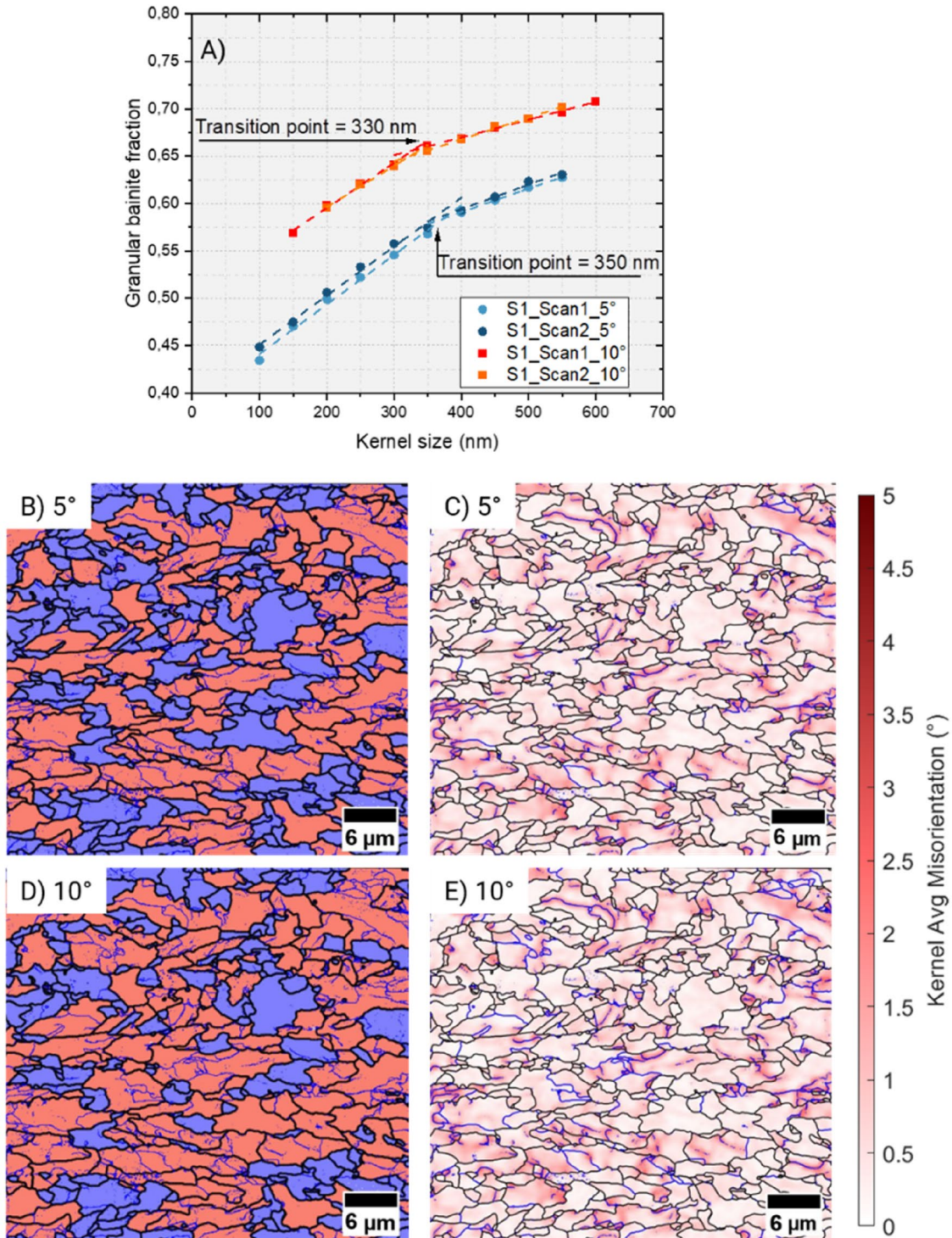


**Figure 5:** (A) Granular bainite fraction vs. kernel size using a grain tolerance angle of 5° (blue data) and 10° (red data), respectively. A transition point at 350 nm and 330 nm was determined by fitting a linear equation to achieve the best R-squared factor. (B) and (C) show a representative classification result and KAM map for the 5° criteria and (D) and (E) represent the result of the 10° criteria. Grain boundaries are highlighted as bold black lines and sub-boundaries as blue lines. Granular bainite is colored orange and polygonal ferrite blue.

kernel size and defined a kernel size of 350 nm to compare the achieved classification results. Subsequently, a granular bainite fraction of 58% and 66% was determined by applying

a grain tolerance angle of 5° and 10°, respectively. Altering the grain tolerance angle from 5° to 10° also changed the average grain size from  $4.2 \pm 0.6 \mu\text{m}$  to  $9.7 \pm 1.0 \mu\text{m}$ . A representative

classification result (granular bainite = orange and polygonal ferrite = blue) and KAM map is shown for both grain tolerance criteria within Fig. 5(B–C) ( $5^\circ$ ) and Fig. 5(D–E) ( $10^\circ$ ). The grain boundaries are highlighted as bold black lines, and the sub-boundaries ( $2^\circ$  to  $5^\circ$ ) are displayed as blue lines. It is evident that the  $10^\circ$  criterion leads to a coarser grain structure in comparison to the  $5^\circ$  criterion. The KAM maps illustrate for both tested grain tolerance angle that grains with sub-boundaries contain localized misorientations next to the sub-grain boundaries and in general a higher, non-uniform misorientation distribution over the residual grain area. Those grains were mainly classified as granular bainite by applying the  $5^\circ$  and  $10^\circ$  criteria. However, the application of both grain tolerance angles resulted in differences in the granular bainite fraction of 8%. In order to clarify the reason which leads to the different classification result, correlative ECCI investigations were conducted.

### Correlative ECCI investigations

Correlative point-to-origin measurements were conducted to determine the orientation gradient within grains which were differently classified using the automated Matlab® code and a grain tolerance angle of  $5^\circ$  and  $10^\circ$ . In contrast to Chen et al. [15], the point-to-origin measurements were not performed over sub-grain boundaries to classify both constituents. The reason is that thermomechanical-treated steels may contain ferrite grains which are subdivided by sub-grain boundaries [24, 40]. A representative result (grain PF-7) of the point-to-origin measurements and its KAM map as well as ECCI image is shown in Fig. 6. In this example, the application of a grain tolerance angle of  $5^\circ$  and  $10^\circ$  led to a different classification of polygonal ferrite and granular bainite, respectively. This

is related to the different grain shape as a result of the different grain tolerance angle and is illustrated by the KAM map [Fig. 6(A–B)]; the small grain boundary part which changes from a sub-boundary (at  $10^\circ$ ) to a grain boundary (at  $5^\circ$ ) is indicated by the violet arrow in Fig. 6(B). The three point-to-origin measurements were carried out within the selected grain as shown by the black, red, and green arrow in Fig. 6(A) and reveal an orientation gradient below  $3^\circ$  for all three measurements [Fig. 6(D)]. Additionally, the ECCI image [Fig. 6(C)] shows that PF-7 has a nearly homogeneous contrast overall the grain area (red-dashed line according to a  $5^\circ$  grain tolerance angle) and does not contain any substructure. Therefore, the additional investigations indicate that the selected grain belongs to the polygonal ferrite phase and thus, the application of a grain tolerance angle of  $5^\circ$  reveals a refined and more accurate phase fraction compared to the  $10^\circ$  criterion. This is in accordance with a previous study which showed that the determined grain tolerance angle of  $5^\circ$  leads to a phase classification which correlates with the mechanical properties [25]. Finally, the investigated HSLA steel consists of 56% granular bainite and 44% of polygonal ferrite according to the automated phase classification system using a grain tolerance angle of  $5^\circ$ . Previous investigations [10, 15, 16] have dealt with similar compositions and revealed comparable phase fractions; however, one should note that the phase fraction also strongly depends on the applied cooling rate, the production parameters, and chemical composition.

The performed nanoindentation tests [Fig. 3(C)] did not allow a clear separation of both constituents according to the average mechanical properties. This could be related to the impact of the substructure within the granular bainite grains [3, 41, 42]. Consequently, further ECCI investigations on

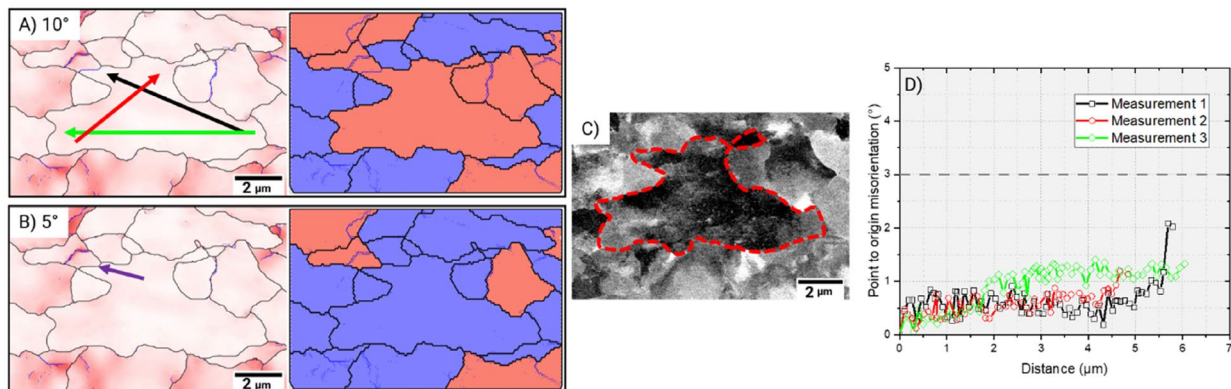


**Figure 6:** Representative result of the additional point-to-origin measurements. The KAM map illustrates the different grain shape using a grain tolerance angle of  $10^\circ$  (A) and  $5^\circ$  (B) which led to a classification as granular bainite (orange) and polygonal ferrite (blue). The violet arrow in (B) highlights the small grain boundary part which changes from a sub-boundary (at  $10^\circ$ ) to a grain boundary (at  $5^\circ$ ); grain boundaries are highlighted as black and sub-boundaries as blues lines. The ECCI image of the representative grain is shown in (C) and reveals no substructure inside (the red-dashed line shows the grain boundary according to a  $5^\circ$  grain tolerance angle). All three point-to-origin measurements (D) (as indicated by the black, red, and green arrow in (A)) classified the selected grain as polygonal ferrite due to an orientation gradient  $< 3^\circ$ .



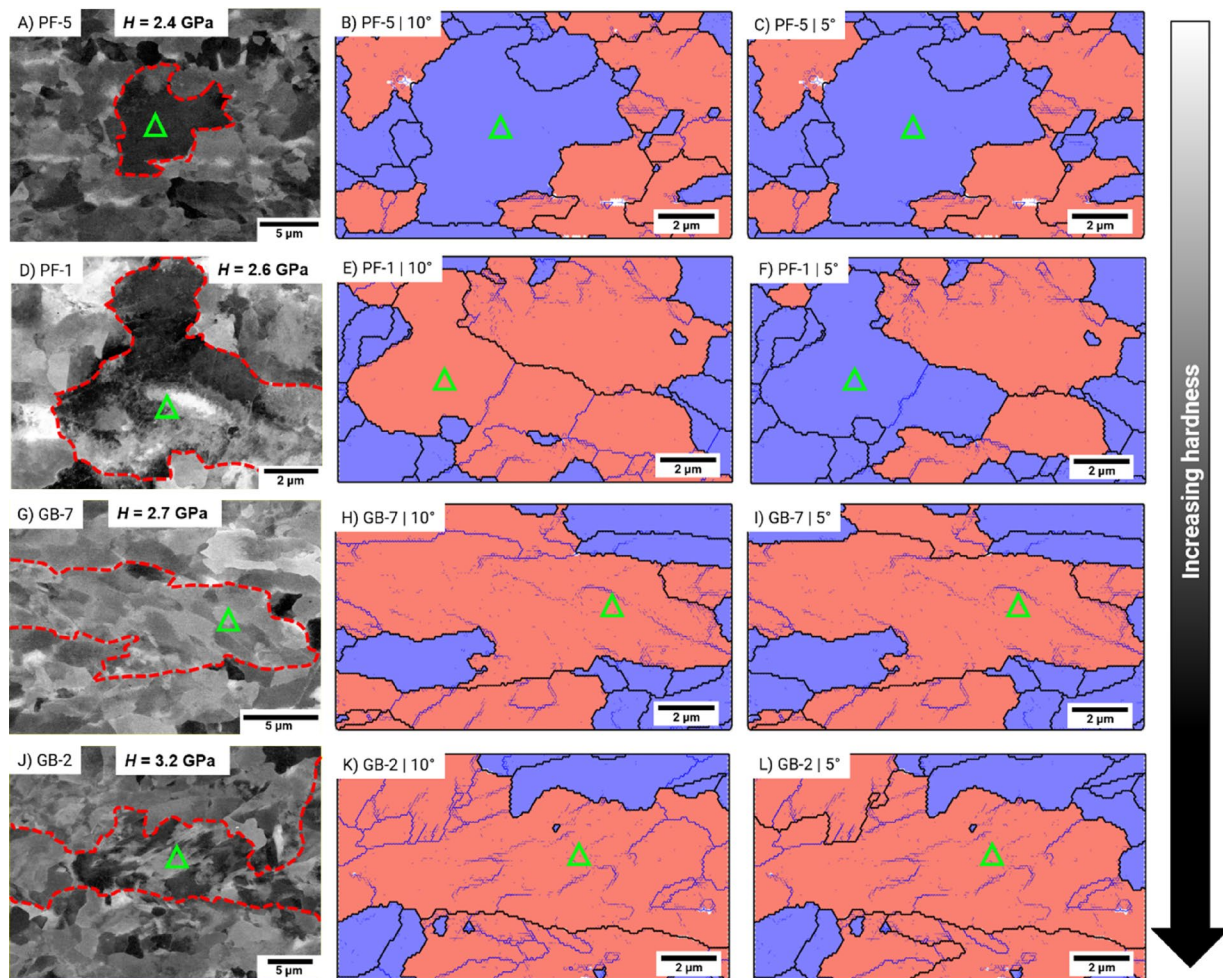


**Figure 7:** Four representative grains of each category are illustrated by their ECCI image (A, D, G, J). The red-dashed line within the ECCI images represent the grain boundary ( $5^\circ$ ). Those grains were classified using the automated phase classification system and a grain tolerance angle of  $10^\circ$  (B, E, H, K) and  $5^\circ$  (C, F, I, L). The used grain tolerance angle is given within the EBSD classification result; grain- and sub-boundaries are displayed as black and blue lines, respectively. The green triangle within all images illustrate the approximate indent position.

different polygonal ferrite and granular bainite grains were conducted to reveal the influencing aspects which caused the overlapping mechanical properties.

### Mechanical properties of four different grain categories

By comparing the substructures in the ECCI images with the classification map, four grain categories can be classified. This is illustrated by the four examples shown in Fig. 7. The grain boundaries ( $5^\circ$ ) are displayed as red-dashed lines within the ECCI images and the green triangle indicates the approximate position of a nanoindent which was made after imaging. The first category represents grains which were classified as polygonal ferrite by both grain tolerance angle criteria and does not show any evidence of substructures in the ECCI image [Fig. 7(A–C)]. From nanoindentation, a hardness value of 2.4 GPa was determined for this polygonal ferrite grain.

The algorithm, however, assigns different classification results in the second group [Fig. 7(D–F)]. Indeed, grain PF-1 contains also an internal strain like the second category and leads to a discontinuous ECCI contrast from the top to the bottom region of the grain. By further tilting of the sample, it is confirmed that the contrast continuously changed and no substructure could be identified. In terms of hardness, PF-1 has a value of 2.6 GPa and is comparable to granular bainite grains with a coarse substructure (third category). Consequently, the second category comprises polygonal ferrite grains which contain a large internal strain which may result in a higher hardness approaching granular bainite. Therefore, the internal strain inside polygonal ferrite leads to a classification failure of 8% using a grain tolerance angle of  $10^\circ$  [see Fig. 5(A)]. The internal strain in such cases can affect the whole grain area but can be also concentrated within a small part of the grain. A possible reason that leads to the strain gradient inside some

polygonal ferrite grains could be the onset of a displacive granular bainite transformation or an inhomogeneous deformation during the rolling process [3, 9, 24].

In contrast to the second category, a subset of ECCI images exhibited grains with a coarser substructure and a smaller internal distortion as shown in Fig. 7(G–I). Such grains were identified as granular bainite by both grain tolerance angles and represents the third category due to a hardness of 2.7 GPa. Comparable to the third category, the fourth category contains grains which are identified as granular bainite for grain tolerance angles of both 5° and 10° [Fig. 7(J–L)]. This category is characterized by a fine substructure separated by sub-boundaries. Additionally, those grains show in the ECCI image [Fig. 7(J)] an inhomogeneous contrast due to a large internal distortion. In contrast to Fig. 7(G–I), the granular bainite grain GB-2 with the finer substructure reached a hardness of 3.2 GPa.

In general, it has been shown that the displacive transformation subdivides the prior austenite grain into packets which are separated into blocks and again into small bainite laths [9, 43]. The lower cooling, which has to be used to form granular bainite instead of upper or lower bainite, forms a substructure with a misorientation distribution of 2° to 15° [36]. Due to the high angular resolution of the backscatter detector (0.28–0.57°), it is possible to resolve the granular bainite substructure [44]. As the ECCI images in Fig. 7(G) and (J) show, the granular bainite substructure size is not equal between the two representative grains and leads to a lower hardness in the case of a coarser substructure. It has been found that the effective lath size is proportional to the mechanical properties of the granular bainite grain [25]. Consequently, the smaller substructure of the fourth category

leads to higher hardness values compared to the third category. A changing substructure size can partly be caused by a different prior austenite grain size, where smaller austenite grains form a smaller substructure [45]. In addition, the substructure size also changes during the continuous cooling process; the higher the transformation temperature, the coarser the substructure size. In contrast to the nanoindentation tests, the automated classification system was able to identify both categories as granular bainite (with the 5° and 10° grain tolerance angle).

Hence, the same average hardness values summarized in Table 1 were achieved due to the different categories of each constituent with minor differences in terms of mechanical properties. Thus, it is crucial to consider the different grain categories to achieve an average hardness of each constituent, since the determined categories are not strictly separated. This means that the mechanical properties of the individual categories overlap due to a continuous transition of the granular bainite substructure and orientation gradient within polygonal ferrite grains. Therefore, it is challenging to characterize both constituents using nanoindentation tests only. Consequently, the correlative investigation between EBSD and ECCI revealed that the application of a grain tolerance angle of 5° is able to more accurately separate grains and achieved the best coincidence.

### Influencing aspects

It has been observed that the point-to-origin measurement can reveal a misleading identification within grains of the second category. Figure 8(A) illustrates the position/direction of two point-to-origin measurements within PF-1 (second category)

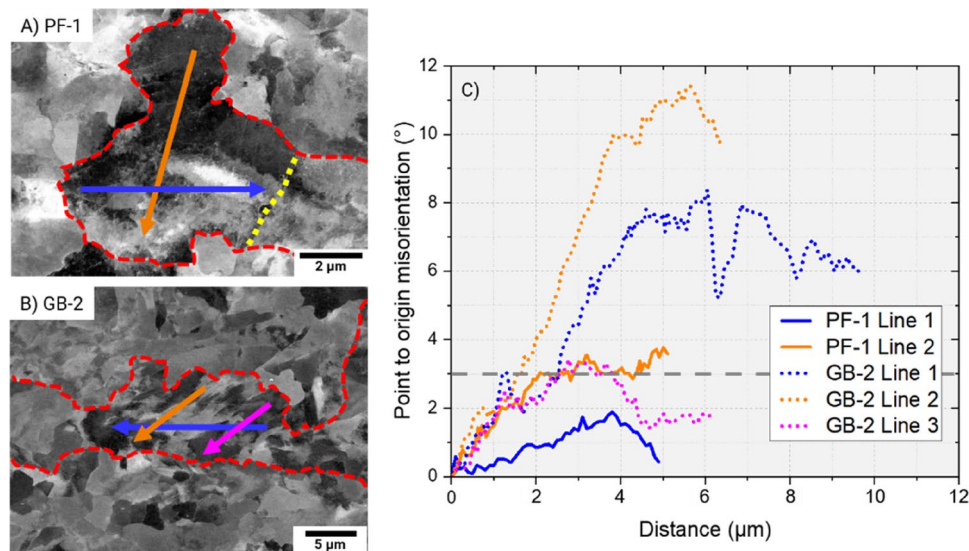


**Figure 8:** ECCI image of PF-1 (A) and GB-2 (B) where the arrows indicate the position and direction of the point-to-origin measurement (blue, orange, and magenta). The grain boundary (grain tolerance angle 5°) is indicated as red-dashed line and the sub-boundary in (A) as yellow-dotted line. The results of the point-to-origin measurement is shown in (C).

and exhibits a misorientation below  $3^\circ$  according to the first measurement [PF-1 Line 1 in Fig. 8(C)]. The second measurement (PF-1 Line 2) contradicts to the first result and reveals an orientation gradient above  $3^\circ$ . According to the ECCI investigations, PF-1 was classified as polygonal ferrite since a substructure was not revealed by continuously tilting of the sample [see Fig. 7(D)]. In comparison to the second category, granular bainite grains of the third and fourth categories showed a misorientation above  $3^\circ$  irrespective of the measurement direction/position as displayed by the three measurements in Fig. 8(B–C). Therefore, the orientation gradient within polygonal ferrite grains aggravates the phase classification and highlights the difficulties to distinguish polygonal ferrite from granular bainite according to point-to-origin measurements. Thus, the automated KAM classification system offers an improved phase classification, since it was shown that an orientation gradient within polygonal ferrite grains can affect the phase differentiation by point to origin. Hence, several point-to-origin measurements would be required to reduce this impact if they were to be performed. It is worth to note that the EBSD-KAM phase classification result depends on the predetermination of the right misorientation angle.

As already described, granular bainite consists of irregular ferrite and a carbon-rich second phase as degenerated pearlite or martensite retained austenite [1]. The LOM images in Fig. 2(A) revealed that the studied material contained both constituents which were not separately classified by the automated classification system. The carbon-rich second phase has not been separately considered, since these particles are located next to grain boundaries and possess a comparable image quality to pixels within granular bainite grains [46]. Thus, grains connected with parts of the carbon-rich second phase may be classified as granular bainite and tend to increase the granular bainite fraction. This is related to the lattice distortion of the carbon-rich constituents and can cause a KAM value above  $3^\circ$  [47].

Another aspect that should not be neglected which influences the automated classification is the strain accumulation toward sub-boundaries. It has been frequently observed that deformed materials exhibit a strain localization and consequently higher KAM values in the vicinity of sub-boundaries [48–50]. Wright et al. [51] demonstrated that this may not only be attributed to the pile-up of dislocations but also to a loss of diffraction pattern precision, since the diffraction volume contains the lattice information of both grains when the electron beam is placed near or on the boundary. Therefore, care has to be taken when a strain localization is measured near grain boundaries by EBSD but where the ECCI analysis does not resolve a substructure within the residual grain. So far, this aspect has not been considered for the automated classification system and further investigations are needed. In addition, the microstructure characterization could be

also influenced by the observed crystallographic orientation, since a higher or lower orientation gradient may be measured depending on the plane of view. In such a case, ECCI can be used to fine tune the KAM classification criteria.

## Conclusion

In this study, different techniques were used to qualify and quantify the phase fractions of granular bainite and polygonal ferrite in an HSLA steel and determine their benefits and limitations. More specifically, we adopted all structural (EBSD-KAM), mechanical (nanoindentation), and chemical investigation (ToF-SIMS) approaches correlatively on the same investigated regions. The Matlab® toolbox MTEX has been utilized to develop an automated classification system using a KAM threshold of  $3^\circ$  to separate both constituents. For the first time, the revealed results were validated by ECCI studies and compared with the performed nanoindentation tests. It has been shown that the automated classification system is able to achieve a reliable classification and agrees with the ECCI investigations. An optimal kernel size of 350 nm and a grain tolerance angle of  $5^\circ$  were determined to achieve the best phase separation. By correlative EBSD and ECCI investigations, the microstructures can be subdivided into two main and four sub categories, which themselves correlate well with nanoindentation responses. The first category is purely polygonal ferrite grains with a homogeneous channeling contrast over the entire grain area, and the nanohardness is about 2.4 GPa. The second category is more ambiguous; although regarded as polygonal ferrite grains (based on in-depth observation using ECCI), an existing internal strain (gradient) and a similar hardness level as granular bainite grains of the third category lead to a misclassification as bainitic phases. This is further compounded by the inability of ToF-SIMS to resolve the minute chemical differences between phases. The third and fourth categories feature granular bainite grains yet with different substructure sizes, and the detected hardness were 2.7 GPa and 3.2 GPa, respectively. Due to the continuous transition between all four grain categories and the orientation gradient within polygonal ferrite grains of the second category, a phase classification by nanoindentation was impeded. The differences between the four categories are correlated to substructure size and the effective grain size determining the mechanical properties and agrees well with previous investigations. Finally, a phase fraction of 56% granular bainite and 44% polygonal ferrite was calculated according to the automated phase classification system. While this is a big step forward in discriminating similar phases in steels, complex multiphase steels still need further research on automated phase classification to allow reliable phase discrimination beyond expert evaluation of LOM and SEM images.

## Material and methods

### Material and microstructural characterization

All investigations were carried out on a HSLA steel with a chemical composition of Fe–0.05C–0.32Si–1.45Mn (in wt.%) and additions of Cu, Ni, Nb, and Ti. The sample was thermomechanically rolled, followed by an accelerated cooling. The material was cut into pieces of  $7 \times 5 \times 3$  mm, ground, and mechanically polished by a suspension containing 30-nm alumina particles (OPA). The microstructure was revealed using a 1% nital solution and light optical microscopy (LOM). A Zeiss Auriga® dual-beam FIB with a Ga<sup>+</sup> ion source was used to mark  $80 \times 80 \mu\text{m}^2$  areas on each sample for correlative investigations. These areas were also measured by EBSD; details about the EBSD parameters are mentioned in “Automated EBSD phase identification and quantification” section. The substructure of the selected regions was investigated using a Zeiss Merlin® SEM combined with a backscattered electron detector. An acceleration voltage 30 kV was applied to perform ECCI investigations. The nanoindentation tests were performed and analyzed according to the Oliver and Pharr method [52] with a commercial nanoindentation system (Hysitron TriboIndenter 950). Selected grains were tested using a Bruker diamond Berkovich indenter geometry. The tip had an effective radius of 200 nm and was loaded with a maximum force of 4.5 mN, using a loading/hold/unloading time of 10 s/5 s/10 s, respectively. All experiments were load controlled and the Berkovich geometry was calibrated against fused silica before testing the sample.

ToF-SIMS was performed on a TOF-SIMS5 instrument (ION-TOF GmbH, Münster, Germany) equipped with a Bi cluster primary ion source and a reflectron-type time-of-flight analyzer. UHV base pressure during analysis was  $1 \times 10^{-10}$  mbar. Mass-scale calibration was based on low-molecular weight hydrocarbon signals. Before imaging the samples were cleaned in vacuo by applying a 500-eV Cs beam up to a dose density of  $6 \times 10^{15}$  ions/cm<sup>2</sup> under SIMS monitoring. For imaging the burst alignment mode was applied proving an un-bunched Bi<sub>3</sub><sup>+</sup>, 25 keV, primary ion beam. In total 300 scans, cycle time 50  $\mu\text{s}$ , with  $512 \times 512$  pixel were recorded on a  $100 \times 100 \mu\text{m}^2$  field of view showing easily the FIB markings on the sample for guidance. Due to the long recording time of 64 min thermal drifts in the spectrometer can cause shifts. These shifts, in the range of up to approx. 10 pixels were compensated by post-processing the data. Therefore, the strong O<sup>-</sup> images recorded were binned into pairs of two and referenced to the previous scans (ION-TOF SurfaceLab version 7.2.129059).

### Automated EBSD phase identification and quantification

The basis for the automated phase identification system is provided by the obtained EBSD data. To quantify the phase fraction, two representative  $80 \times 80 \mu\text{m}^2$  scan areas were considered. The measurements were conducted with an EDAX® Hikari detector;

a step size of 50 nm and an acceleration voltage of 20 kV were chosen. The EDAX® software TSL OIM Analysis 8 and the Matlab® toolbox MTEX were utilized to analyze the exported .ang-files obtained from the EBSD measurement [39]. A grain dilation clean-up with a tolerance angle of 5° and a minimum grain size of 3 pixel was performed on all EBSD scans to reduce the impact of incorrectly indexed pixels; no more than 5% of the pixels were changed. Subsequently, the MTEX program calculates the KAM for the defined kernel size for each pixel and classifies each grain as granular bainite once the KAM is above 3°. Finally, MTEX creates a colormap of the used EBSD file and directly calculates the phase fraction. Investigations conducted to reveal a reliable automated phase classification included the following parameters:

- *Grain tolerance angle* defines the threshold until which angle neighboring pixels are grouped together to the same grain;
- *Kernel size* is calculated by the following equation:  $(n\text{-th nearest neighbor}) \times (\text{step size})$  and takes all  $n$  neighbors into account;
- *KAM angle* defines the threshold until which neighbors are considered with a misorientation angle smaller than the selected *KAM angle* [39].

An orientation gradient of 3° was used as threshold to distinguish granular bainite and polygonal ferrite grains, based on Ref. [15]. Consequently, the developed program classifies grains as granular bainite once the calculated KAM of a pixel exceeds a misorientation of 3°, otherwise it will be classified as polygonal ferrite. Both constituents contain low angle grain boundaries (LAGBs) to accommodate the shape change during the controlled hot deformation process (polygonal ferrite) and the onset of displacive transformation (granular bainite) [15, 24]. Thus, the *KAM angle* was set to 4.9° to reduce the impact of low angle grain boundaries on the constituent classification. The impact of the grain tolerance angle and the kernel size was characterized by varying them in the range of 5° and 10° to distinguish sub- and grain boundaries as well as using different kernel sizes ranging from 100 to 600 nm. The MTEX code applied is given in the “Supplementary Information”.

### Point-to-origin measurements of misorientation

In contrast to Chen et al. [15], the point-to-origin measurements were not performed over sub-grain boundaries identified by EBSD to classify both constituents. It has been shown that thermomechanically-treated steels may contain ferrite grains which are subdivided by sub-grain boundaries [24, 40]. Moreover, three point-to-origin measurements were carried out in different directions and at different positions within each selected grain. It was necessary that all three point-to-origin

measurements reached values below  $3^\circ$  to classify the tested grain as polygonal ferrite. “Influencing aspects” section explains this criterion in detail.

## Acknowledgments

The authors gratefully acknowledge the funding of this project and for supplying the sample material by the steel manufacturer AG der Dillinger Hüttenwerke. C.K. and G.D. are also grateful for the financial support of the German Research Foundation (Deutsche Forschungsgemeinschaft, DFG) within the Collaborative Research Center (TRR 188, “Damage Controlled Forming Processes,” 278868966) in project B03 “Understanding the damage initiation at microstructural scale.” S.P.T. acknowledges the funding support numbered 111L7499 from the National Taiwan University.

## Funding

Open Access funding enabled and organized by Projekt DEAL.

## Data availability

The raw data/processing data required to reproduce these results cannot be shared at this time.

## Declarations

**Conflict of interest** To the authors’ best knowledge, no potential conflicts of interest exist.

## Open Access

This article is licensed under a Creative Commons Attribution 4.0 International License, which permits use, sharing, adaptation, distribution and reproduction in any medium or format, as long as you give appropriate credit to the original author(s) and the source, provide a link to the Creative Commons licence, and indicate if changes were made. The images or other third party material in this article are included in the article’s Creative Commons licence, unless indicated otherwise in a credit line to the material. If material is not included in the article’s Creative Commons licence and your intended use is not permitted by statutory regulation or exceeds the permitted use, you will need to obtain permission directly from the copyright holder. To view a copy of this licence, visit <http://creativecommons.org/licenses/by/4.0/>.

## Supplementary Information

The online version contains supplementary material available at <https://doi.org/10.1557/s43578-023-01113-7>.

## References

1. S. Zajac, V. Schwinn, K.H. Tacke, Characterisation and quantification of complex bainitic microstructures in high and ultra-high strength linepipe steels. *Mater. Sci. Forum* **500–501**, 387–394 (2005). <https://doi.org/10.4028/www.scientific.net/msf.500-501.387>
2. Z.J. Xie, X.P. Ma, C.J. Shang, X.M. Wang, S.V. Subramanian, Nano-sized precipitation and properties of a low carbon niobium micro-alloyed bainitic steel. *Mater. Sci. Eng. A* **641**, 37–44 (2015). <https://doi.org/10.1016/j.msea.2015.05.101>
3. S. Jun Jia, B. Li, Q. You Liu, Y. Ren, S. Zhang, H. Gao, Effects of continuous cooling rate on morphology of granular bainite in pipeline steels. *J. Iron Steel Res. Int.* **27**, 681–690 (2020). <https://doi.org/10.1007/s42243-019-00346-3>
4. W.B. Lee, S.G. Hong, C.G. Park, S.H. Park, Carbide precipitation and high-temperature strength of hot-rolled high-strength, low-alloy steels containing Nb and Mo. *Metall. Mater. Trans. A Phys. Metall. Mater. Sci.* **33**, 1689–1698 (2002). <https://doi.org/10.1007/s11661-002-0178-2>
5. G. Krauss, S.W. Thompson, Ferritic microstructures in continuously cooled low- and ultralow-carbon steels. *ISIJ Int.* **35**, 937–945 (1995). <https://doi.org/10.2355/isijinternational.35.937>
6. T.N. Baker, Microalloyed steels. *Ironmak. Steelmak.* **43**, 264–307 (2016). <https://doi.org/10.1179/1743281215Y.0000000063>
7. S.W. Thompson, D.J. Vin Col, G. Krauss, Continuous cooling transformations and microstructures in a low-carbon, high-strength low-alloy plate steel. *Metall. Trans. A* **21**, 1493–1507 (1990). <https://doi.org/10.1007/BF02672564>
8. B.X. Wang, X.H. Liu, G.D. Wang, Correlation of microstructures and low temperature toughness in low carbon Mn–Mo–Nb pipeline steel. *Mater. Sci. Technol.* **29**, 1522–1528 (2013). <https://doi.org/10.1179/1743284713Y.0000000326>
9. H.K.D.H. Bhadeshia, *Bainite in Steels: Theory and Practice* (CRC Press, Boca Raton, 2019)
10. B.M. Huang, J.R. Yang, H.W. Yen, C.H. Hsu, C.Y. Huang, H. Mohrbacher, Secondary hardened bainite. *Mater. Sci. Technol.* **30**, 1014–1023 (2014). <https://doi.org/10.1179/1743284714Y.0000000536>
11. C.N. Hulme-Smith, I. Lonardelli, M.J. Peet, A.C. Dippel, H.K.D.H. Bhadeshia, Enhanced thermal stability in nanostructured bainitic steel. *Scr. Mater.* **69**, 191–194 (2013). <https://doi.org/10.1016/j.scriptamat.2013.03.029>
12. R.Y. Zhang, J.D. Boyd, Bainite transformation in deformed austenite. *Metall. Mater. Trans. A Phys. Metall. Mater. Sci.* **41**, 1448–1459 (2010). <https://doi.org/10.1007/s11661-010-0190-x>
13. M.C. Zhao, K. Yang, F.R. Xiao, Y.Y. Shan, Continuous cooling transformation of undeformed and deformed low carbon pipeline steels. *Mater. Sci. Eng. A* **355**, 126–136 (2003). [https://doi.org/10.1016/S0921-5093\(03\)00074-1](https://doi.org/10.1016/S0921-5093(03)00074-1)

14. H.J. Jun, J.S. Kang, D.H. Seo, K.B. Kang, C.G. Park, Effects of deformation and boron on microstructure and continuous cooling transformation in low carbon HSLA steels. *Mater. Sci. Eng. A* **422**, 157–162 (2006). <https://doi.org/10.1016/j.msea.2005.05.008>
15. Y.W. Chen, Y.T. Tsai, P.Y. Tung, S.P. Tsai, C.Y. Chen, S.H. Wang, J.R. Yang, Phase quantification in low carbon Nb-Mo bearing steel by electron backscatter diffraction technique coupled with kernel average misorientation. *Mater. Charact.* **139**, 49–58 (2018). <https://doi.org/10.1016/j.matchar.2018.01.041>
16. Y.W. Chen, B.M. Huang, Y.T. Tsai, S.P. Tsai, C.Y. Chen, J.R. Yang, Microstructural evolutions of low carbon Nb/Mo-containing bainitic steels during high-temperature tempering. *Mater. Charact.* **131**, 298–305 (2017). <https://doi.org/10.1016/j.matchar.2017.07.022>
17. M. Müller, D. Britz, L. Ulrich, T. Staudt, F. Mücklich, Classification of bainitic structures using textural parameters and machine learning techniques. *Metals* **10**, 1–19 (2020). <https://doi.org/10.3390/met10050630>
18. S.C. Wang, J.R. Yang, Effects of chemical composition, rolling and cooling conditions on the amount of martensite/austenite (M/A) constituent formation in low carbon bainitic steels. *Mater. Sci. Eng. A* **154**, 43–49 (1992). [https://doi.org/10.1016/0921-5093\(92\)90361-4](https://doi.org/10.1016/0921-5093(92)90361-4)
19. J. Wu, P.J. Wray, C.I. Garcia, M. Hua, A.J. Deardo, Image quality analysis: A new method of characterizing microstructures. *ISIJ Int.* **45**, 254–262 (2005). <https://doi.org/10.2355/isijinternational.45.254>
20. E. Keehan, L. Karlsson, H.K.D.H. Bhadeshia, M. Thuvander, Electron backscattering diffraction study of coalesced bainite in high strength steel weld metals. *Mater. Sci. Technol.* **24**, 1183–1188 (2008). <https://doi.org/10.1179/174328407X226572>
21. S.I. Wright, M.M. Nowell, D.P. Field, A review of strain analysis using electron backscatter diffraction. *Microsc. Microanal.* **17**, 316–329 (2011). <https://doi.org/10.1017/S1431927611000055>
22. L. Ryde, Application of EBSD to analysis of microstructures in commercial steels. *Mater. Sci. Technol.* **22**, 1297–1306 (2006). <https://doi.org/10.1179/174328406X130948>
23. S. Zaefferer, P. Romano, F. Friedel, EBSD as a tool to identify and quantify bainite and ferrite in low-alloyed Al-TRIP steels. *J. Microsc.* **230**, 499–508 (2008). <https://doi.org/10.1111/j.1365-2818.2008.02010.x>
24. P. Cizek, The microstructure evolution and softening processes during high-temperature deformation of a 21Cr-10Ni-3Mo duplex stainless steel. *Acta Mater.* **106**, 129–143 (2016). <https://doi.org/10.1016/j.actamat.2016.01.012>
25. K. Zhu, O. Bouaziz, C. Oberbillig, M. Huang, An approach to define the effective lath size controlling yield strength of bainite. *Mater. Sci. Eng. A* **527**, 6614–6619 (2010). <https://doi.org/10.1016/j.msea.2010.06.061>
26. B.-W. Choi, D.-H. Seo, J. Jang, A nanoindentation study on the micromechanical characteristics of API X100 pipeline steel. *Met. Mater. Int.* **15**, 373–378 (2009). <https://doi.org/10.1007/s12540-009-0373-4>
27. R.M. Jentner, K. Srivastava, S. Scholl, F.J. Gallardo-Basile, J.P. Best, C. Kirchlechner, G. Dehm, Unsupervised clustering of nanoindentation data for microstructural reconstruction: Challenges in phase discrimination. *Materialia* **28**, 101750 (2023). <https://doi.org/10.1016/j.mtla.2023.101750>
28. T. Yamashita, Y. Tanaka, M. Nagoshi, K. Ishida, Novel technique to suppress hydrocarbon contamination for high accuracy determination of carbon content in steel by FE-EPMA. *Sci. Rep.* **6**, 29825 (2016). <https://doi.org/10.1038/srep29825>
29. P.T. Pinard, A. Schwedt, A. Ramazani, U. Prah, S. Richter, Characterization of dual-phase steel microstructure by combined sub-micrometer EBSD and EPMA carbon measurements. *Microsc. Microanal.* **19**, 996–1006 (2013). <https://doi.org/10.1017/S1431927613001554>
30. S. Eswara, A. Pshenova, E. Lentzen, G. Nogay, M. Lehmann, A. Ingenito, Q. Jeangros, F.-J. Haug, N. Valle, P. Philipp, A. Hessler-Wyser, T. Wirtz, A method for quantitative nanoscale imaging of dopant distributions using secondary ion mass spectrometry: An application example in silicon photovoltaics. *MRS Commun.* **9**, 916–923 (2019). <https://doi.org/10.1557/mrc.2019.89>
31. M. Kubicek, G. Holzlechner, A.K. Opitz, S. Larisegger, H. Hutter, J. Fleig, A novel ToF-SIMS operation mode for sub 100nm lateral resolution: Application and performance. *Appl. Surf. Sci.* **289**, 407–416 (2014). <https://doi.org/10.1016/j.apsusc.2013.10.177>
32. B. Josefsson, H.-O. Andrén, Microstructure of granular bainite. *Le Journal de Physique Colloques* **49**, 293–298 (1988). <https://doi.org/10.1051/jphyscol:1988651>
33. H. Bhadeshia, R. Honeycombe, *Steels: Microstructure and Properties* (Butterworth-Heinemann, Boston, 2017)
34. F.G. Caballero, H. Roelofs, S. Hasler, C. Capdevila, J. Chao, J. Cornide, C. Garcia-Mateo, Influence of bainite morphology on impact toughness of continuously cooled cementite free bainitic steels. *Mater. Sci. Technol.* **28**, 95–102 (2012). <https://doi.org/10.1179/1743284710Y.0000000047>
35. D. De-Castro, A. Eres-Castellanos, J. Vivas, F.G. Caballero, D. San-Martín, C. Capdevila, Morphological and crystallographic features of granular and lath-like bainite in a low carbon microalloyed steel. *Mater. Charact.* **184**, 111703 (2022). <https://doi.org/10.1016/j.matchar.2021.111703>
36. W.C. Jeong, Microstructural aspects of quasi-polygonal and granular bainitic ferrites in an ultra-low-carbon interstitial-free high-strength steel. *Metall. Mater. Trans. A* **34**, 2025–2026 (2003). <https://doi.org/10.1007/s11661-003-0167-0>
37. S. Zaefferer, J. Ohlert, W. Bleck, A study of microstructure, transformation mechanisms and correlation between microstructure

- and mechanical properties of a low alloyed TRIP steel. *Acta Mater.* **52**, 2765–2778 (2004). <https://doi.org/10.1016/j.actamat.2004.02.044>
38. B.L. Bramfitt, J.G. Speer, A perspective on the morphology of bainite. *Metall. Trans. A* **21**, 817–829 (1990). <https://doi.org/10.1007/BF02656565>
  39. F. Bachmann, R. Hielscher, H. Schaeben, Texture analysis with MTEX-free and open source software toolbox. *Solid State Phenom.* (2010). <https://doi.org/10.4028/www.scientific.net/SSP.160.63>
  40. B. Eghbali, A. Abdollah-Zadeh, H. Beladi, P.D. Hodgson, Characterization on ferrite microstructure evolution during large strain warm torsion testing of plain low carbon steel. *Mater. Sci. Eng. A* **435–436**, 499–503 (2006). <https://doi.org/10.1016/j.msea.2006.07.026>
  41. T.B. Britton, D. Randman, A.J. Wilkinson, Nanoindentation study of slip transfer phenomenon at grain boundaries. *J. Mater. Res.* **24**, 607–615 (2009). <https://doi.org/10.1557/jmr.2009.0088>
  42. W.A. Soer, K.E. Aifantis, J.T.M. De Hosson, Incipient plasticity during nanoindentation at grain boundaries in body-centered cubic metals. *Acta Mater.* **53**, 4665–4676 (2005). <https://doi.org/10.1016/j.actamat.2005.07.001>
  43. T. Furuhashi, H. Kawata, S. Morito, T. Maki, Crystallography of upper bainite in Fe-Ni-C alloys. *Mater. Sci. Eng. A* **431**, 228–236 (2006). <https://doi.org/10.1016/j.msea.2006.06.032>
  44. S. Zaeferrer, N.N. Elhami, Theory and application of electron channelling contrast imaging under controlled diffraction conditions. *Acta Mater.* **75**, 20–50 (2014). <https://doi.org/10.1016/j.actamat.2014.04.018>
  45. S. Morito, H. Saito, T. Ogawa, T. Furuhashi, T. Maki, Effect of austenite grain size on the morphology and crystallography of lath martensite in low carbon steels. *ISIJ Int.* **45**, 91–94 (2005). <https://doi.org/10.2355/isijinternational.45.91>
  46. J.M. Reichert, M. Militzer, W.J. Poole, L. Collins, A new approach using EBSD to quantitatively distinguish complex transformation products along the HAZ in X80 Linepipe steel, in: Volume 3: Materials and Joining; Risk and Reliability, American Society of Mechanical Engineers, 2014: pp. 1–7. <https://doi.org/10.1115/IPC2014-33668>.
  47. H. Terasaki, Y.I. Komizo, Morphology and crystallography of bainite transformation in a single prior-austenite grain of low-carbon steel. *Metall. Mater. Trans. A Phys. Metall. Mater. Sci.* **44**, 2683–2689 (2013). <https://doi.org/10.1007/s11661-013-1610-5>
  48. S.K. Mishra, P. Pant, K. Narasimhan, A.D. Rollett, I. Samajdar, On the widths of orientation gradient zones adjacent to grain boundaries. *Scr. Mater.* **61**, 273–276 (2009). <https://doi.org/10.1016/j.scriptamat.2009.03.062>
  49. C. Perrin, S. Berbenni, H. Vehoff, M. Berveiller, Role of discrete intragranular slip on lattice rotations in polycrystalline Ni: Experimental and micromechanical studies. *Acta Mater.* **58**, 4639–4649 (2010). <https://doi.org/10.1016/j.actamat.2010.04.033>
  50. A.D. Rollett, F. Wagner, N. Allain-Bonasso, D.P. Field, R.A. Lebensohn, Comparison of gradients in orientation and stress between experiment and simulation. *Mater. Sci. Forum* **702–703**, 463–468 (2011). <https://doi.org/10.4028/www.scientific.net/MSF.702-703.463>
  51. S.I. Wright, M.M. Nowell, R. De Kloe, L. Chan, Orientation precision of electron backscatter diffraction measurements near grain boundaries. *Microsc. Microanal.* **20**, 852–863 (2014). <https://doi.org/10.1017/S143192761400035X>
  52. W.C. Oliver, G.M. Pharr, An improved technique for determining hardness and elastic modulus using load and displacement sensing indentation experiments. *J. Mater. Res.* **7**, 1564–1583 (1992). <https://doi.org/10.1557/JMR.1992.1564>

**Publisher's Note** Springer Nature remains neutral with regard to jurisdictional claims in published maps and institutional affiliations.